J. Fluid Mech. (1998), *vol.* 365, *pp.* 205–234. Printed in the United Kingdom

Significance of the dispersed-phase viscosity on the simple shear flow of suspensions of two-dimensional liquid drops

By RICHARD CHARLES AND C. POZRIKIDIS

Department of Applied Mechanics and Engineering Sciences, University of California, San Diego, La Jolla, CA 92093-0411, USA
e-mail: costas@ames.ucsd.edu

(Received 30 January 1997 and in revised form 27 January 1988)

The significance of drop-fluid viscosity on the effective rheological properties and on the dynamics of the microstructure of mono-disperse suspensions of two-dimensional liquid drops with constant interfacial tension is investigated by means of numerical simulations at vanishing Reynolds number, using the boundary integral method for Stokes flow. Three important features of the numerical method are the computation of the doubly-periodic Green's function and associated stress tensor by tabulation and interpolation, the iterative solution of a deflated integral equation for the interfacial velocity, and the repositioning of the drop interfaces at close proximity to avoid artificial coalescence. In the first part of the simulations, the interaction of two intercepting drops in simple shear flow is studied in an extended range of conditions, and the results are used to quantify the behaviour and develop insights into the physics of dilute systems. In the second part of the simulations, the motion of a random suspension of 25 drops repeated periodically in the two spatial directions is studied at the areal fraction $\phi = 0.30$, drop fluid to ambient fluid viscosity ratio $\lambda = 1$ or 10, and drop capillary number $Ca = 0.10$ or 0.30, a total of four combinations. It is found that the rheological properties of the suspension and the average drop deformation and orientation depend on the values of λ and Ca in a subtle fashion. As the viscosity of the drops is raised, the drop-centre pair distribution function undergoes a transition from a liquid-like to a rigid-particle-like behaviour, and particle aggregation and cluster formation become more important. For $\lambda = 10$, the results are in excellent qualitative, and in some cases quantitative, agreement with those presented in previous studies for mono-layered suspensions of rigid spheres. The drop self-diffusivity is computed and its dependence on λ and Ca is discussed, although the results carry some uncertainty owing to the moderate number of drops within each periodic cell.

1. Introduction

In a recent article (Li, Charles & Pozrikidis 1996), we presented results of dynamical simulations of the flow of two-dimensional, mono-disperse, random suspensions of deformable liquid drops in simple shear flow. In the parametric studies, the motion of a doubly-periodic suspension containing 25 or 49 drops per periodic cell was simulated using the boundary integral method for Stokes flow. Because of high computational cost, the viscosity of the drop was restricted to that of the ambient fluid. The investigations illustrated the effects of the areal fraction of the suspended phase and of the capillary number expressing the drop deformability, on (i) the effective rheological

properties of the suspension, (ii) the evolution of the microstructure described in terms of the drop shape, orientation, and relative position, and (iii) the motion of the individual drops in the context of hydrodynamic self-diffusivity. Toose (1997) carried out similar simulations with 24 drops per periodic cell over a broader range of areal fractions and capillary numbers, and confirmed and extended the rheological data of Li *et al*. (1996).

Loewenberg & Hinch (1996) presented a similar numerical investigation of the analogous but more realistic problem in three dimensions. Because of high computational cost, the maximum number of drops in each periodic box was 12, which is adequate for deducing the rheological properties of a non-dilute suspension, but not so large as to permit the investigation of the statistical properties of the evolving microstructure with reasonable confidence. In fact, only a few drops per cell are needed to deduce the rheological properties of a suspension within tolerable error. Loewenberg & Hinch's investigation included a parametric study of the effect of the ratio of the drop to ambient fluid viscosity λ, for $\lambda \leqslant 5$. Their results for $\lambda = 1$ were in qualitative agreement with those reported by Li *et al*. (1996), and this suggests similarities in the nature of the two- and three-dimensional flow. In a more recent study, Loewenberg & Hinch (1997) considered the interaction of two intercepting three-dimensional drops in infinite shear flow, and extracted information on the hydrodynamic drop diffusivity in a dilute suspension.

One important difference between the two- and three-dimensional flow concerns the breakup of narrow threads extracted from highly extended drops owing to the Rayleigh capillary instability, but such disfigured shapes did not arise in the simulations. Another difference concerns the nature of drop collision and interface coalescence: the lubrication forces in two-dimensional flow are considerably stronger than those in three-dimensional flow. The interfacial deformability in both cases, however, causes the formation of an interfacial dimple and accompanying coalescing rim, and renders the three-dimensional and the two-dimensional motions similar at near interface contact.

The numerical simulations of Loewenberg & Hinch (1996) established that the particle fluidity expressed by the viscosity ratio λ has an important effect on the rheological properties of a suspension. However, the precise way in which λ affects the motion of a drop through the suspension, and the manner in which a collection of drops arrange themselves in the flow have been discussed only in qualitative ways. For example, highly viscous drops and drops of any viscosity whose interfaces have been immobilized by surfactants are expected to stay close together for a long period of time during interception, and this allows clusters to form. In contrast, drops with low viscosity and mobile interfaces can effectively slide and roll over each other, and this prevents aggregation. Indeed, Li *et al*. (1996) and Loewenberg & Hinch (1996) found that cluster formation is not definitive in suspensions of liquid drops with $\lambda = 1$ with fully mobile interfaces with constant surface tension. On the contrary, cluster formation in suspensions of rigid particles has been observed in the laboratory and demonstrated in the simulations beyond any doubt.

Another effect of the viscosity ratio λ concerns the stability of the interfaces and the integrity of the suspended drops. During the flow, parts of the interfaces are subjected to a local shearing motion which makes them susceptible to sustained oscillations due to viscosity variations at sufficiently high capillary numbers. Although it is unlikely that such oscillations will alter the global properties of the suspension in a fundamental way at low and moderate shear rates, it is nevertheless likely to play an important role in the stability of the dispersed phase under conditions of extreme deformation.

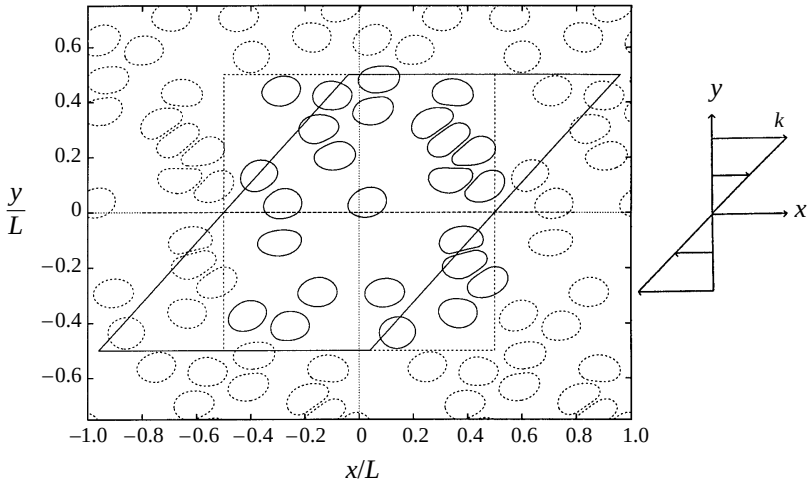

FIGURE 1. Instantaneous configuration of a suspension of drops subject to simple shear flow along the x-axis with velocity $u_x = ky$, showing the initial square and sheared periodic box.

Apart from the global rheological properties, an important aspect of a suspension flow concerns the description of the individual particle motions in terms of a hydrodynamic diffusivity tensor, defined in terms of the rate of change of the dyadic variance of the particle centre displacement. Recent contributions to the theory and computation of the self-diffusivity of rigid and deformable particles in dense or dilute suspensions were made by Da Cunha & Hinch (1996), Morris & Brady (1996), Madanshetty, Nadim & Stone (1996), Wang, Mauri & Acrivos (1996), Loewenberg & Hinch (1996), and by a multitude of authors who contributed to a workshop dedicated to this subject (Davis 1996). Li *et al.* (1996) confirmed that the seemingly random motion of a drop in a suspension with $\lambda = 1$ can be described in terms of an effective self-diffusivity tensor, computed the transverse component of this tensor, and discussed its dependence on the deformability of the interfaces expressed by the capillary number. The self-diffusivity in a non-dilute suspension for $\lambda \neq 1$ has not been discussed in previous studies.

In this work, we investigate the influence of interfacial deformability and particle fluidity on the flow of non-dilute suspensions of liquid drops in simple shear flow. The numerical studies are similar to those performed by Loewenberg & Hinch (1996, 1997) for the analogous problem in three dimensions, and extend those of Li *et al.* (1996) and Toose (1997) to $\lambda \neq 1$. Consideration of the two-dimensional flow has the benefit that the motion of a larger number of particles can be tracked for a longer period of time, and the statistical properties of the microstructure and the apparently diffusive motion of the individual drops can be assessed with less uncertainty. The maximum number of drops employed in the present simulations is 25, which is still moderate and thus barely enough for computing the self-diffusivity with tolerable error. Some trends may nevertheless be deduced with reasonable confidence.

The numerical simulations are carried out by the boundary-integral method for Stokes flow, which we have previously referred to as the method of *interfacial dynamics* by analogy with the method of *contour dynamics* for vortex flow. Three important features of the numerical method, to be discussed in subsequent sections, are: computation of the doubly-periodic Green's function of Stokes flow and its associated stress tensor by tabulation and interpolation; complete deflation of the integral

equation to allow for an iterative solution; and repositioning of interfaces at low separations to prevent artificial coalescence.

2. Problem formulation

We consider the motion of a two-dimensional, doubly-periodic, mono-disperse suspension of neutrally buoyant liquid drops with equivalent radius a and viscosity $\lambda\mu$, suspended in an ambient liquid with viscosity μ. The drops translate and deform under the influence of a simple shear flow directed along the x-axis with velocity $\boldsymbol{u}^{\infty} = (ky, 0)$, where k is the constant shear rate, as depicted in figure 1. The flow pattern replicates itself in the directions of two base vectors $\boldsymbol{a}_1$ and $\boldsymbol{a}_2$ that are convected by the unperturbed simple shear flow. At the initial instant, the base vectors are chosen to lie along the x- and y-axes and their lengths are equal to L. Thus the area of a periodic cell is and remains equal to L^2.

At the origin of computational time, we randomly distribute N identical circular drops within each periodic box and, assuming that inertial effects are negligible, we compute their subsequent motion by solving the equations of Stokes flow (e.g. Pozrikidis 1997). Using the boundary-integral formulation, we find that the velocity at a point $\boldsymbol{x}_0$ that lies on an interface can be computed by solving the integral equation

$$u_j(\boldsymbol{x}_0) = \frac{1}{1+\lambda}\delta_{jx}ky_0 - \frac{1}{2\pi\mu(1+\lambda)}\sum_{l=1}^{N}\int_{D_l}\Delta f_i(\boldsymbol{x})\,G_{ij}(\boldsymbol{x},\boldsymbol{x}_0)\,\mathrm{d}l(\boldsymbol{x}) + \frac{1}{2\pi}\frac{1-\lambda}{1+\lambda}\sum_{l=1}^{N}{}^{PV}\int_{D_l} u_i(\boldsymbol{x})\,T_{ijk}(\boldsymbol{x},\boldsymbol{x}_0)\,n_k(\boldsymbol{x})\,\mathrm{d}l(\boldsymbol{x}), \quad (2.1)$$

where D_l stands for the interface of the lth drop in a periodic box, the tensor $\boldsymbol{G}$ is the doubly-periodic Green's function for the equations of Stokes flow with vanishing flow rate across each face of a periodic cell, and $\boldsymbol{T}$ is the corresponding stress tensor. Expressions for $\boldsymbol{G}$ and $\boldsymbol{T}$ in terms of Ewald sums are presented by Pozrikidis (1996), van de Vorst (1996), and Charles (1997). The quantity $\Delta\boldsymbol{f}$ in the first integral on the right-hand side of equation (2.1) is the jump in traction across the interfaces. In the case of liquid drops with constant surface tension γ, $\Delta\boldsymbol{f} = \gamma\kappa\boldsymbol{n}$, where κ is the curvature of a drop interface in the (x, y)-plane, and $\boldsymbol{n}$ is the unit vector normal to the interface pointing into the ambient fluid.

Non-dimensionalizing all variables using the equivalent drop radius a as the characteristic length, the inverse shear rate $1/k$ as the characteristic time, ka as the characteristic velocity, and μk as the characteristic stress, we find that the motion of the suspension depends on the drop capillary number $Ca = \mu ka/\gamma$, the viscosity ratio λ, the areal fraction $\phi = N\pi a^2/L^2$, the number of drops per periodic cell N, and the distribution of the drops at the initial instant. In §5, we shall present numerical results for $\phi = 0.30$ and $N = 25$, and for two combinations fo values of Ca and λ.

In subsequent sections, we shall describe the shape of the individual drops in terms of (i) the deformation parameter of an individual D, defined as $D = (A-B)/(A+B)$ where A and B are the maximum and minimum drop dimension, and (ii) the orientation angle α subjected between the longest drop axis and the x-axis.

The rheological properties of the suspension will be described in terms of the areal-average value of the stress tensor, designated with pointed brackets, which can be placed in the form

$$\langle\sigma_{ij}\rangle = -\delta_{ij}\langle p\rangle + 2\mu\langle e_{ij}\rangle + \sigma^P_{ij}, \quad (2.2)$$

where $\boldsymbol{e}$ is the rate of deformation tensor. The effect of the suspended phase is manifested in the particle stress tensor σ^p defined as

$$\sigma_{ij}^P = \frac{1}{L^2}\sum_{l=1}^{N} \int_{D_l} \Delta f_i(\boldsymbol{x})\, x_j \,\mathrm{d}l(\boldsymbol{x}) - \mu(1-\lambda)\frac{1}{L^2}\sum_{l=1}^{N} \int_{D_l} (u_i(\boldsymbol{x})\, n_j(\boldsymbol{x}) + u_j(\boldsymbol{x})\, n_i(\boldsymbol{x}))\,\mathrm{d}l(\boldsymbol{x}). \quad (2.3)$$

For liquid drops with constant interfacial tension γ, the first integral on the right-hand side of (2.3) may be expressed in the computationally preferred form $2\boldsymbol{\Sigma}^{(l)}$, where

$$\Sigma_{ij}^{(l)} = \tfrac{1}{2}\gamma \int_{D_l} t_i(\boldsymbol{x})\, t_j(\boldsymbol{x})\,\mathrm{d}l(\boldsymbol{x}) \quad (2.4)$$

is the interfacial energy tensor, and $\boldsymbol{t}$ is the unit vector tangential to the interface pointing in the counterclockwise direction (Zhou & Pozrikidis 1993*b*). This form makes the symmetry of the particle stress tensor apparent.

A simple computation exploiting the periodicity condition shows that the diagonal elements of $\langle \boldsymbol{e} \rangle$ vanish, and the off-diagonal elements are equal to $\frac{1}{2}k$. Accordingly, we define the effective viscosity of the suspension μ_{eff} in terms of the relation

$$k\mu_{eff} = \langle \sigma_{xy} \rangle. \quad (2.5)$$

To further characterize the motion of the suspension, we introduce the first normal-stress difference

$$N_{eff} = \langle \sigma_{xx} \rangle - \langle \sigma_{yy} \rangle. \quad (2.6)$$

A positive value of N_{eff} indicates that the suspension behaves like a polymeric solution with some elastic properties.

To study the statistics of the relative position of the centres of two drops, we introduce the pair distribution function $g(r, \theta)$, which is defined in terms of the probability density function that the centre of a drop is located within a small area centred at the radial and angular positions r and θ, while a test drop is located at the origin; the probability density function is then normalized by the particle number density N/L^2 to yield $g(r, \theta)$ (e.g. Hansen & McDonald 1986). The integral of $g(r, \theta) - 1$ over the whole area of the flow is constant, equal to zero at all times. Peaks and valleys in the graph of $g(r, \theta)$ reflect the presence of ordered structure.

Finally, we introduce the number-averaged mean drop-cluster size

$$\langle s \rangle = \sum_s s n_s \Big/ \sum_s n_s, \quad (2.7)$$

where n_s is the number of drops that form an s-sized cluster. The computation of n_s will be discussed in § 5.4.

3. Numerical method

The numerical method is similar to that developed by Li *et al.* (1996). An important new feature is the iterative solution of an integral equation (2.1) for the interfacial velocity. Previously, we stipulated $\lambda = 1$ and obtained an integral representation; thus, it was not necessary to solve an integral equation. To make the computational cost affordable, it is imperative to solve the integral by an iterative method, and we chose the simplest method of successive substitutions implemented by Jacobi or Gauss–Siedel iterations.

We found that as the number of drops N is increased, or the viscosity ratio λ is raised, or two interfaces come close to one another, the number of iterations necessary

to reach a specified level of accuracy becomes larger. There are critical thresholds of N and λ where the iterations diverge even though the interfaces have perfectly circular shapes. In theory, the iterations should converge for any number of drops and for any non-zero and non-infinite value of λ (e.g. Pozrikidis 1992), but, in practice, the integral operators lose compactness owing to the various numerical approximations. The iterations can be made to converge by introducing a larger number of marker points around each interface or by applying a higher-order scheme for computing the interfacial integrals, but the numerical method is no longer affordable. With 25 randomly distributed circular drops and 32 points around each interface, we could not obtain a convergent solution for λ outside the window of (0.5, 3).

To circumvent this stumbling block, we applied the method of eigenvalue deflation described by Pozrikidis (1992, pp. 124–126) for three-dimensional flow and by Zhou & Pozrikidis (1993*a*) for two-dimensional flow in a channel with a single interface. Considering the mth interface, we introduce three normalized eigenfunctions of the double-layer potential expressing rigid body motion, given by

$$\boldsymbol{q}^{(m,1)} = \frac{1}{\beta_{m,1}}\boldsymbol{e}_x, \quad \boldsymbol{q}^{(m,2)} = \frac{1}{\beta_{m,2}}\boldsymbol{e}_y, \quad \boldsymbol{q}^{(m,3)} = \frac{1}{\beta_{m,3}}\boldsymbol{e}_z \times (\boldsymbol{x} - \boldsymbol{X}^{(m)}), \tag{3.1}$$

where $\boldsymbol{e}_x, \boldsymbol{e}_y, \boldsymbol{e}_z$, are the unit vectors along the x-, y-, and z-axes, and $\boldsymbol{X}^{(m)}$ is the centroid of the mth interface. The normalization constants $\beta_{m,i}$ are computed so that the eigenfunctions satisfy the orthonormalization constraint

$$\int_{D_m} q_k^{(m,i)} q_k^{(m,j)} \, \mathrm{d}l = \delta_{ij} \tag{3.2}$$

for i or $j = 1, 2, 3$. Next, for a point $\boldsymbol{x}_0$ that lies at the mth interface, we replace the integral equation (2.1) with the following integral equation for an artificial velocity-like variable $\boldsymbol{v}$:

$$\begin{aligned} v_j(\boldsymbol{x}_0) = {} & \frac{1}{1+\lambda} k y_0 \, \delta_{jx} - \frac{1}{2\pi\mu(1+\lambda)} \sum_{l=1}^{N} \int_{D_l} \Delta f_i(\boldsymbol{x}) \, G_{ij}(\boldsymbol{x}, \boldsymbol{x}_0) \, \mathrm{d}l(\boldsymbol{x}) \\ & + \frac{1-\lambda}{1+\lambda} \, \frac{1}{2\pi} \sum_{l=1}^{N} \, {\int\!\!\!\!\!\!-}_{D_l} v_i(\boldsymbol{x}) \, T_{ijk}(\boldsymbol{x}, \boldsymbol{x}_0) \, n_k(\boldsymbol{x}) \, \mathrm{d}l(\boldsymbol{x}) \\ & + \sum_{k=1}^{3} q_j^{(m,k)}(\boldsymbol{x}_0) \int_{D_m} q_i^{(m,k)}(\boldsymbol{x}) \, v_i(\boldsymbol{x}) \, \mathrm{d}l(\boldsymbol{x}) - \frac{1}{L_m} n_j(\boldsymbol{x}_0) \int_{D_m} v_i(\boldsymbol{x}) \, n_i(\boldsymbol{x}) \, \mathrm{d}l(\boldsymbol{x}) \quad , \end{aligned} \tag{3.3}$$

where L_m is the total arclength of the mth interface. Having computed the solution of (3.3) by the method of successive substitutions, we produce the interfacial velocity by setting

$$\boldsymbol{u} = \boldsymbol{v} - \tfrac{1}{2}(1-\lambda) \sum_{k=1}^{3} \boldsymbol{q}^{(m,k)} \int_{D_m} q_i^{(m,k)}(\boldsymbol{x}) \, v_i(\boldsymbol{x}) \, \mathrm{d}l(\boldsymbol{x}). \tag{3.4}$$

Charles (1997) proves that equations (3.3) and (3.4) imply the original equation (2.1).

That the deflation was implemented correctly was confirmed by ensuring that the original and deflated systems produce identical solutions. Enabling the deflation reduces the number of necessary iterations by a large factor, in some cases by a factor of one hundred. We must emphasize again that deflation is imperative, not merely an option; without it, we would not have been able to carry out the simulations.

An important practical feature of the numerical method is the computation of the doubly-periodic Green's function $\boldsymbol{G}$ and associated stress tensor $\boldsymbol{T}$ by tabulation and interpolation. The symmetries of these tensors are fully exploited to reduce the size of

the look-up tables. The non-singular parts of $\boldsymbol{G}$ and $\boldsymbol{T}$ were tabulated as functions of the x-component of the base vector $\boldsymbol{a}_2$, denoted as a_{21}, and of the relative x- and y-positions of the singular and field points, using the interpolation variables $(x-x_0)/L$, $(y-y_0)/L$, and a_{21}/L. For the computation of $\boldsymbol{G}$, the interpolation space was discretized into a three-dimensional $129\times65\times129$ grid. The maximum absolute error due to the interpolation was determined to be of the order of 10^{-5} over the domain of independent variables. For the computation of $\boldsymbol{T}$, memory considerations required an interpolation grid of reduced size $129\times129\times32$. The absolute error due to the tabulation was also found to be of the order 10^{-5}. The accuracy of the interpolation was confirmed by performing several tests where the motion was computed with the Green's function evaluated directly or by interpolation, and ensuring that the results are identical within the expected numerical error. For $\lambda\neq1$, the interpolation of the stress tensor alone reduced the computational cost by a factor of approximately one hundred for a suspension with 25 drops.

When the viscosity ratio is of the order of unity or higher, and the capillary number is sufficiently small so that the particles are not notably deformable, the system of ordinary differential equations descending from the boundary integral formulation is stiff. As a result, a very small timestep is required to describe accurately the motion during the rolling of two drops at interception. In the computations of Li *et al.* (1996) for $\lambda=1$, the timestep at the lowest capillary number considered was set automatically using an error estimator that is inherent in the RKF23 method (e.g. Pozrikidis 1998). If the timestep is not decreased to a sufficiently small level during these critical stages of the motion, the interfaces coalesce in an unphysical fashion. In solving the integral equation (2.1) for $\lambda\neq1$, two troublesome types of behaviour were found to occur. First, if two drop interfaces are close but not touching, the iterations converge so slowly that they fail to meet the preset convergence criteria. Secondly, if the interpolated profiles of the drops actually overlap, the iterations diverge. In either case, the exploratory step involved in the adaptive timestepping method where the truncation error is estimated and the size of timestep is determined, could not be completed.

A very small timestep is thus required at combined conditions of high viscosity ratio and low or moderate capillary numbers, but cannot be afforded in the parametric studies. As a compromise, we implemented a method that repositions the interfaces of two intercepting drops at close proximity, in a manner that keeps them apart during these critical stages of the motion. The method and its consequences on the character of the motion are discussed in the Appendix and in more detail by Charles (1997). For $\lambda=1$, this modification yielded a speed-up factor of approximately 5 for a test with three drops, where one drop touches the other two drops. For $\lambda\neq1$, the modification was the only practical approach for obtaining converged solutions. It is interesting to note that the same general approach forms the basis for detecting holes in meshes of chimera overlapping grids produced by the PEGSUS grid generation program (Suhs & Tramel 1991). A similar regularization scheme was used in the numerical method of Bossis & Brady (1984), and its consequences were discussed by Dratler & Schowalter (1996).

4. Two-drop interactions

A brief examination of the nature of two-drop interactions allows us to develop insights into the elementary motions governing the behaviour of dilute systems, and is a natural prelude to the large-scale simulations with 25 drops.

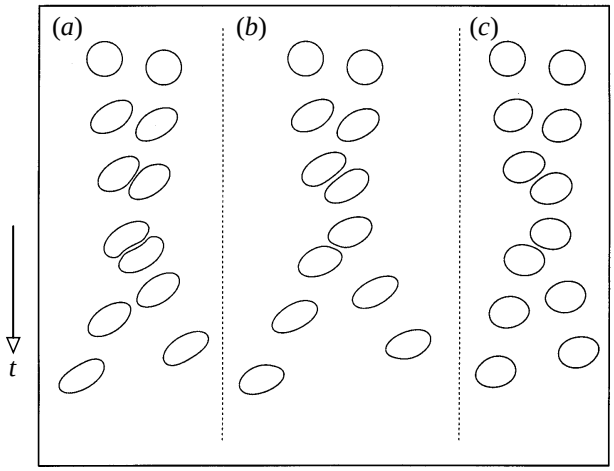

FIGURE 2. Two-drop interactions: sequences of drop profiles during first crossing for $Ca = 0.3$ and (a) $\lambda = 0.05$, (b) 1.0, (c) 10, at times $kt = 0.0$, 2.0, 4.5, 7.0, 9.5 and 12.0.

Figure 2 illustrates the interaction of a pair of drops for $a/L = 0.15$, $Ca = 0.30$, and $\lambda = 0.05$, 1 and 10, during the first crossing, at $kt = 0$, 2.0, 4.5, 7.0, 9.0 and 12.0. At the initial instant, the drops are separated by the distance $0.5L$ along the x-axis, and their centres are displaced upward or downward in an alternating manner by the distance $\delta = 0.25a$. It is evident that the deformations are more prominent at the lowest value of λ. Figure 3 displays the evolution of the lateral drop centre displacement Δy, deformation parameter D, inclination angle α, and suspension effective viscosity and first normal-stress difference, for $\lambda = 10$. It is instructive to divide the interaction into five stages represented by the five panels shown down the right-hand side of figure 3: far approach (stage 1); near approach (stage 2); crossing (stage 3); near recession (stage 4); far recession (stage 5). The corresponding times are marked on the left-hand panels.

The y-coordinate of the right drop centre displayed in figure 3(a) starts at a relatively low value at far approach (stage 1), reaches a maximum displacement at crossing (stage 3), and diminishes to a lower value at far recession (stage 5) which is somewhat higher than the initial value at stage 1. The effective viscosity shown in figure 3(d) rises from an initial value at far approach (stage 1) to a peak value just before near approach (stage 2). This peak also corresponds to a maximum drop rotation found at the same time in figure 3(c). The effective viscosity then drops to a minimum at the stage of drop crossing (stage 3). This extreme in the effective viscosity is in concert with a peak in the normal-stress difference. The distortion of the drop interfaces prior to crossing can also be seen in the variation of the drop deformation parameter in figure 3(b), showing that the deformation parameter actually peaks slightly before the crossing at stage 3.

Each drop recovers from the deformations suffered to accommodate the passage of the other. By the time of crossing (figure 3c), the drops have rotated well past their initial orientation, and have reached a maximum clockwise inclination just before near recession (stage 4). This over-rotation is also visible in figure 3(d) as the first peak in the effective viscosity after the crossing (stage 3), just before near recession (stage 4). The drop shapes also rebound reaching a minimum in the drop deformation parameter and a local maximum in the effective viscosity shortly after near recession (stage 4).

Normalized suspension properties for the three cases $\lambda = 0.05$, 1, and 10 are plotted in figure 4. The average cluster size plotted in this figure with the solid line serves as

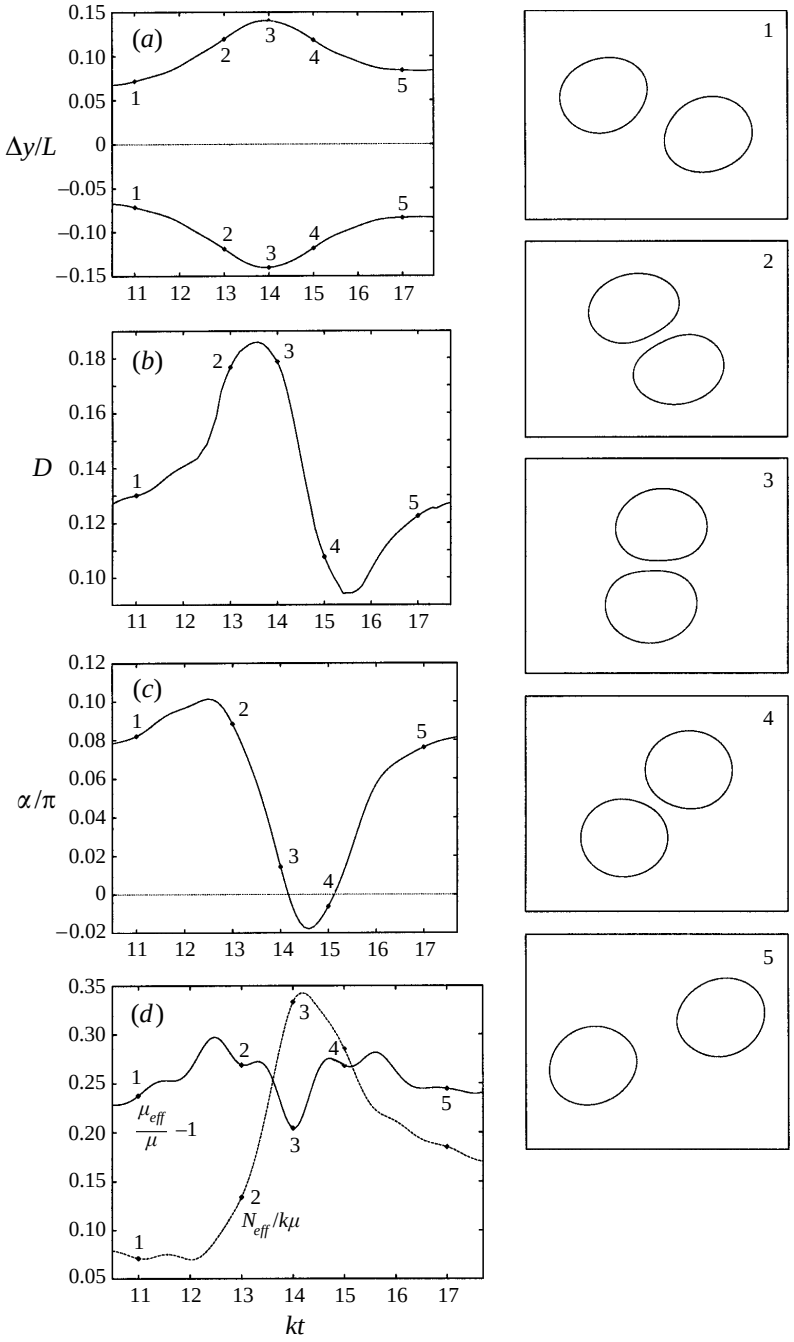

FIGURE 3. Two-drop interactions: suspension properties for $\lambda = 10$ and $Ca = 0.3$. (*a*) Lateral displacement of the drop centres; (*b*) drop deformation parameter; (*c*) drop orientation angle; (*d*) suspension effective viscosity and normal-stress difference. The profiles on the right-hand side correspond to the points marked on the graphs.

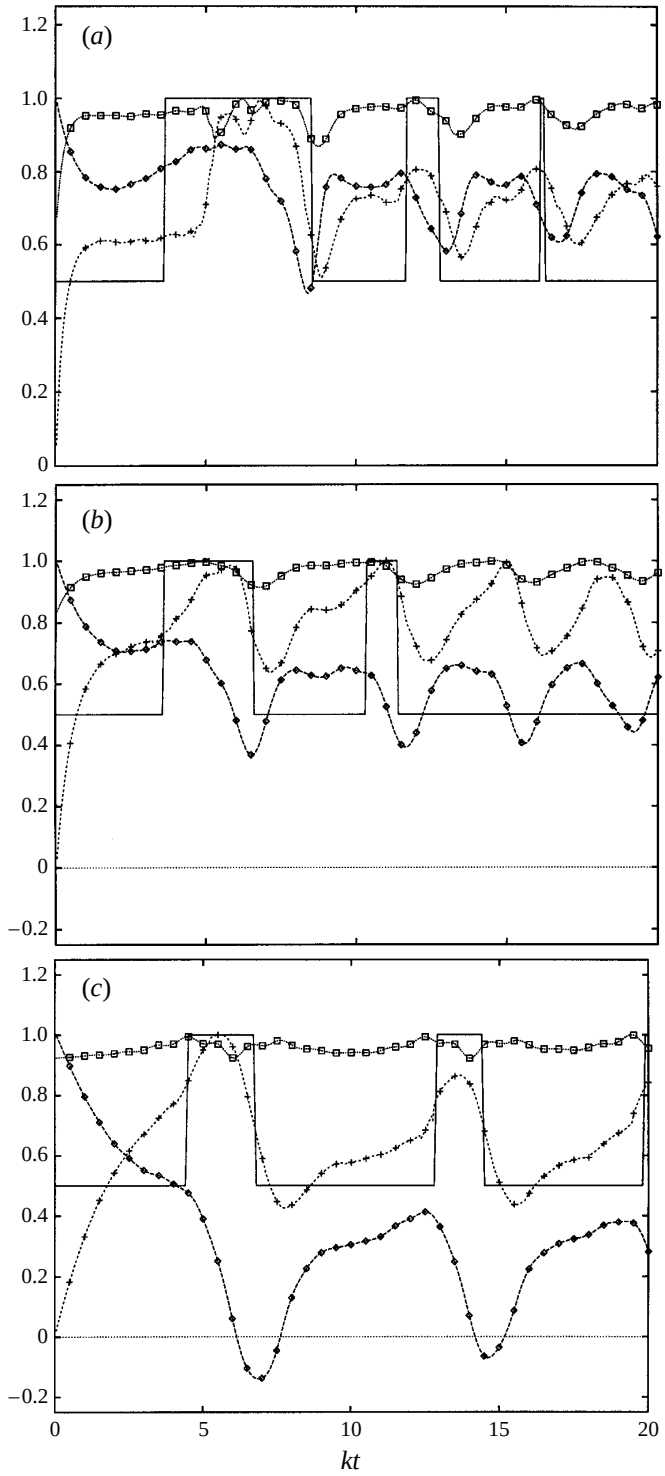

FIGURE 4. Two-drop interactions: suspension properties normalized by the maximum values for the three cases illustrated in figure 2, $Ca = 0.3$ and (*a*) $\lambda = 0.05$, (*b*) 1.0, (*c*) 10. □, μ_{eff}/μ_{max}; +, D/D_{max}; ◇, α/α_{max}; ——, $\langle s\rangle/\langle s\rangle_{max}$.

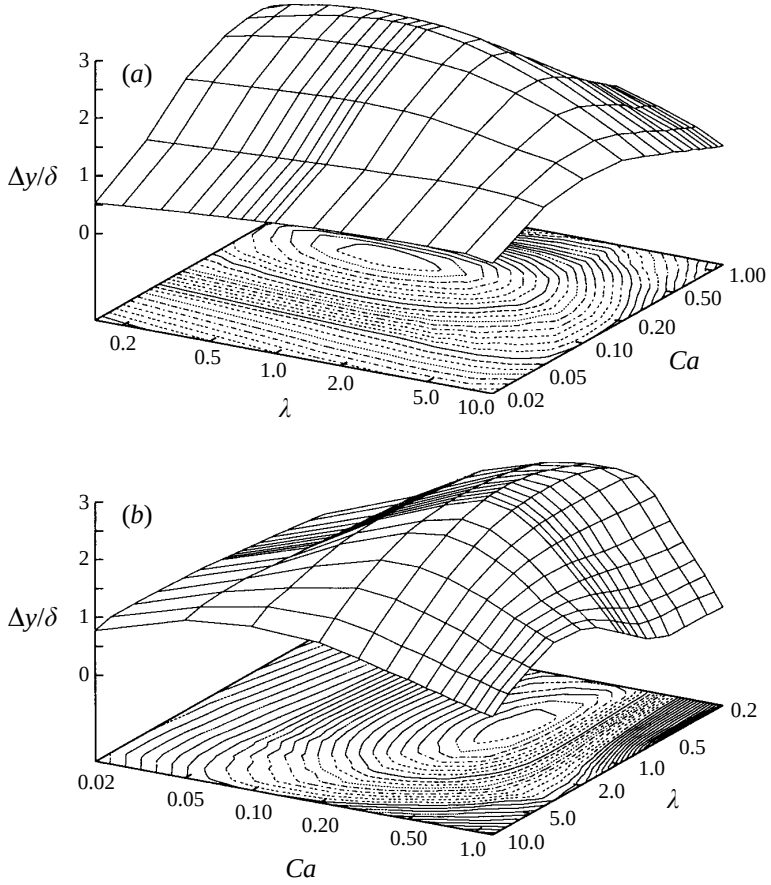

FIGURE 5. Two-drop interactions: the net lateral displacement of two intercepting drops after the first crossing as a function of Ca and λ; δ is the initial drop displacement normal to the x-axis.

a threshold to indicate whether the drops are close enough to be considered as a strongly interacting pair. The effect of the interaction on the rheological parameters for the most deformable drops (figure 4*a*) is manifested in a relatively large window where the drops are close enough to be considered as forming a cluster at the first crossing. At subsequent crossings, the window shrinks considerably. For $\lambda = 1$ corresponding to figure 4(*b*), the interaction window shrinks so rapidly that the cluster size criteria discussed in §5 fail to identify the pair after the second crossing, as the drops have migrated laterally too far. In contrast, for $\lambda = 10$ corresponding to figure 4(*c*), at least three crossings are identified by the windowing threshold of the cluster size criteria. In this case, all three crossings are characterized by first a rise in the effective viscosity, a rapid change in the orientation angle of the drops, and finally a rise and fall of the drop deformation parameter whose peak is centred in the window created by the cluster size threshold.

The combined and individual effects of the viscosity ratio and capillary number on the net displacement after the first crossing, Δy, is illustrated in figure 5 for $a/L = 0.15$ and $\delta/a = 0.25$. Note that the λ and Ca axes are logarithmic. As λ is raised, the drops become less flexible and Δy tends to zero for any value of the capillary number. At high values of Ca, the variation of Δy with λ is non-monotonic, reaching a maximum and a minimum within the range shown in figure 5(*b*). For example, for the three motions

corresponding to $Ca = 0.30$, the lowest displacement occurs when $\lambda = 10$, but the displacement for $\lambda = 1$ is slightly higher than that for $\lambda = 0.05$. Thus the interface deformability allows for the lateral accommodation of two intercepting drops only up to the point where the drops deform so much that the requisite lateral movement of their centroids is diminished. The lateral accommodation is then accomplished not so much by a lateral shift of the centroid, as by the elongation and distortion of the interfaces as they slide by each other in an almost serpentine fashion. The contour plot shown at the base of the plots in figure 5 reveals that maximum lateral displacement over Ca and λ is attained at $Ca \approx 0.3$ and $\lambda \approx 0.7$. These are the sets of conditions at which the drops in a dilute suspension are expected to exhibit the most active motion.

The non-monotonic nature of the lateral displacement values for the two-drop suspension were also observed in simulations of three-dimensional drops by Loewenberg & Hinch (1997). Their figure 7 shows a non-monotonic variation of the cross-flow separation with λ at $Ca = 0.30$, with a minimum occurring somewhere between $\lambda = 4$ and 20. Their figure 10 shows a maximum at $Ca = 0.3$ for $\lambda = 1$. Thus, the simulations of both the two- and three-dimensional flow indicate a region of the (λ, Ca) parameter space of peaked net displacement, invalidating scaling arguments based on volume or areal fraction alone.

5. Simulations with 25 drops

In this section, we present the results of large-scale dynamic simulations with 25 drops, for two values of the viscosity ratio, $\lambda = 1$ and 10, and two values of the capillary number $Ca = 0.1$ and 0.3, a total of four combinations, all for $N = 25$ and areal fraction $\phi = 0.30$. The simulations for $\lambda = 1$ provide us with a frame of reference for assessing the effect of the viscosity ratio. A limited number of simulations were carried out for different values of λ, but the run times were not long enough to justify their discussion. Previous work has shown that the motion for $\lambda = 1$ is typical of that for λ less than roughly 2 (e.g. Loewenberg & Hinch 1996). The value $\phi = 0.30$ expresses the balance of our desire to keep the areal fraction of the dispersed phase as large as possible, so that the suspension is not dilute, and the practical concern that the performance of the numerical method deteriorates, and the computational expense increases drastically, when the interfaces are densely packed.

A fixed reference configuration with 25 randomly distributed circular drops was used as an initial condition in all cases. A second fixed configuration provided us with an alternative initial condition for carrying out confidence tests for each combination. A typical simulation up to the time $kt = 50$ required up to 3 CPU hours on the Cray C90 for $\lambda = 1$, and 45 hours for $\lambda = 10$; this high computational cost explains the scarceness of our case studies. The actual CPU times vary according to the magnitude of drop deformation. Increasing the capillary number allows the interfaces to deform more severely and requires a higher number of interfacial marker points.

In figure 6(a), we depict instantaneous profiles of the interfaces for $\lambda = 1$ and $Ca = 0.10$, at time $kt = 50$. The effect of the capillary number can be deduced by comparing these profiles to those shown in figure 6(b) corresponding to $\lambda = 1$ and $Ca = 0.30$. Greater drop elongations and kidney-shaped interfaces develop during, and even after, drop interception at the higher capillary number. Increasing the viscosity ratio to $\lambda = 10$ causes significant changes in the shapes of the interfaces and on the spatial distribution of the drop centres. Comparing the profiles shown in figure 6(c, d), corresponding to $\lambda = 10$, to those shown in figure 6(a, b) for $\lambda = 1$, we see that the high-viscosity drops have more compact shapes, but occasional large deformations are

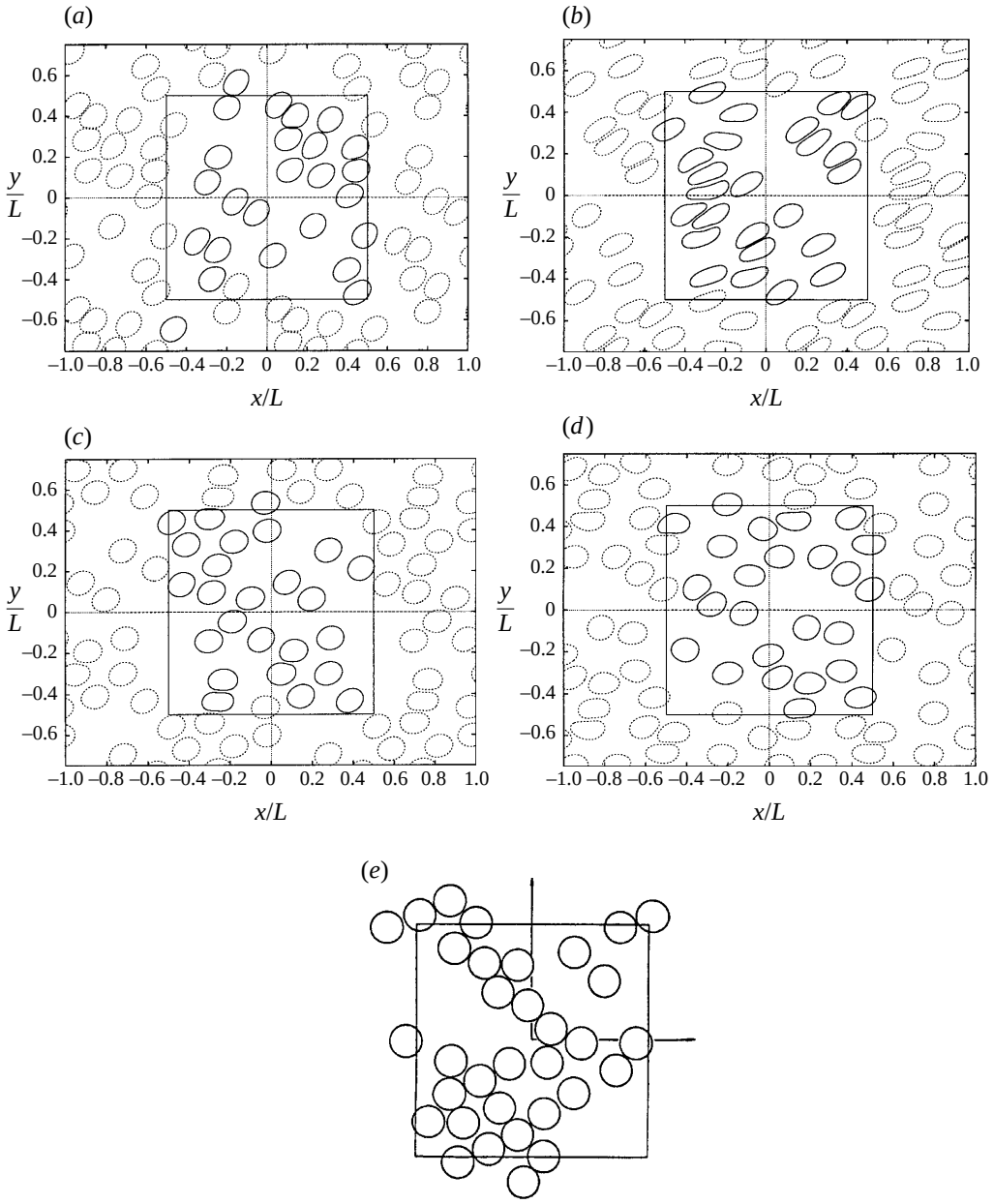

FIGURE 6. Flow of a doubly-periodic suspension with 25 drops per periodic box. Drop interface profiles at $kt = 50$ for (*a*) $\lambda = 1$, $Ca = 0.1$; (*b*) $\lambda = 1$, $Ca = 0.3$; (*c*) $\lambda = 10$, $Ca = 0.1$; (*d*) $\lambda = 10$, $Ca = 0.3$. (*e*) Distribution of rigid spheres in a sheared mono-layered suspension presented by Bossis & Brady (1984); note the similarities with the distribution displayed in (*c*).

observed at the higher capillary number. More importantly, the more viscous drops seem to form linear chains oriented at an angle of 135° with respect to the x-axis. It is furthermore striking to observe the similarities between the configuration shown in figure 6(*c*), and that shown in figure 6(*e*) for a suspension of rigid sphere with volume fraction equal to 0.40, borrowed from Bossis & Brady (1984).

In the next subsections we shall discuss the motion of the suspension in terms of the

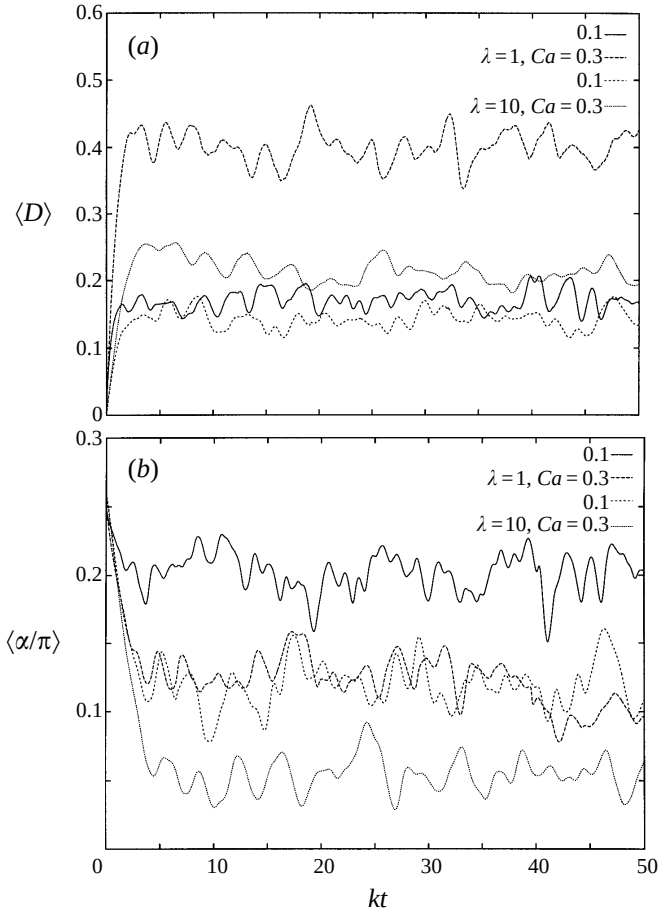

FIGURE 7. Evolution of the suspension mean drop deformation parameter and inclination angle, both averaged over all drops, for the four case studies shown in figure 6.

geometry of the microstructure and the effective rheological properties. Time-average values of time-dependent quantities were computed by integrating over time period from $kt = 10$ to 50, and then taking the mean of the duplicate simulations. The initial period of each simulation was discarded to filter out transient start-up effects. We shall see that the difference in the results of the duplicate simulations corresponding to identical conditions are statistically insignificant compared to the time-average values, and this suggests that the initial state loses its significance after the suspension has evolved for several periods.

5.1. *Average deformation and orientation*

Figure 7(*a*, *b*) illustrates the evolution of the instantaneous drop deformation and inclination, averaged over all drops, for the four case studies considered. In all cases, the mean deformation increases from the value of zero and then fluctuates around well-defined average values. As expected, increasing the capillary number raises the level of the deformation, and the effect is much more pronounced when $\lambda = 1$ than 10. High-viscosity drops take a longer time to respond to fluctuations in the ambient flow. The amplitude of the fluctuations is commensurate with the time-average values. Figure 7(*b*) reveals that the effect of the capillary number on the time-average drop inclination

Ca	λ	Run	$\langle\bar{D}\rangle$	$\langle\bar{\alpha}\rangle/\pi$	$\bar{\mu}_{eff}/\mu$	$\bar{N}_{eff}/\mu k$
0.1	1.0	1	0.170	0.202	1.653	0.400
	1.0	2	0.167	0.200	1.644	0.392
	1.0	Avg	0.169 ± 0.002	0.201 ± 0.001	1.649 ± 0.004	0.396 ± 0.004
	10.0	1	0.143	0.119	1.900	0.783
	10.0	2	0.138	0.115	1.901	0.803
	10.0	Avg	0.141 ± 0.002	0.117 ± 0.002	1.9008 ± 0.0007	0.793 ± 0.01
0.3	1.0	1	0.399	0.121	1.415	0.735
	1.0	2	0.400	0.122	1.421	0.706
	1.0	Avg	0.4002 ± 0.0005	0.1220 ± 0.0001	1.418 ± 0.003	0.72 ± 0.01
	10.0	1	0.215	0.054	1.788	0.495
	10.0	2	0.212	0.056	1.793	0.507
	10.0	Avg	0.214 ± 0.001	0.055 ± 0.002	1.791 ± 0.002	0.501 ± 0.006

TABLE 1. Time-averaged geometrical and rheological properties of random suspensions

Ca	λ	D	α/π
0.1	1.0	0.099	0.217
	10.0	0.071	0.123
0.3	1.0	0.284	0.160
	10.0	0.102	0.054

TABLE 2. Deformation and inclination of a steadily deformed drop in simple shear flow

angle is as strong for $\lambda = 10$ as it is for $\lambda = 1$. In all cases, the drops start elongating at an angle of 45° with respect to the x-axis, and then incline towards it. The large fluctuations are evidence of drop interception and cluster or chain formation. In the computations, the orientation angle is restricted to lie within the window [90°, −90°]. We found that, although some individual drops occasionally rotate to an inclination that is less than zero, the average angle remains positive in all cases.

In the first two columns of table 1, we present the time-average values of the drop deformation and inclination for the individual simulations, as well as their mean values. The trends discussed in the previous paragraphs, and the minor role of the initial configuration, are apparent. In table 2, we present the asymptotic values of the deformation and inclination angle of a steadily deformed drop in simple shear flow, at corresponding conditions. Interestingly, while the average deformation for the suspension is consistently approximately twice that for the solitary drop, the average inclination is remarkably close to that for the solitary drop. This indicates that packing drops in a suspension promotes their overall elongation but does not have a great impact on its orientation; the latter is determined primarily by the strength of the imposed shear flow.

5.2. *Effective rheological properties*

In figure 8(*a*, *b*), we present the evolution of the effective viscosity and first normal stress difference defined in §2. For $\lambda = 1$, the effective viscosity curves rise from the value of unity; for $\lambda = 10$ they rise from a higher value; and in both cases they fluctuate around well-defined mean values. The amplitudes of the fluctuations seem to be insensitive to the physical parameters of the flow. Increasing the capillary number, while holding the viscosity ratio constant, reduces the mean value of the effective

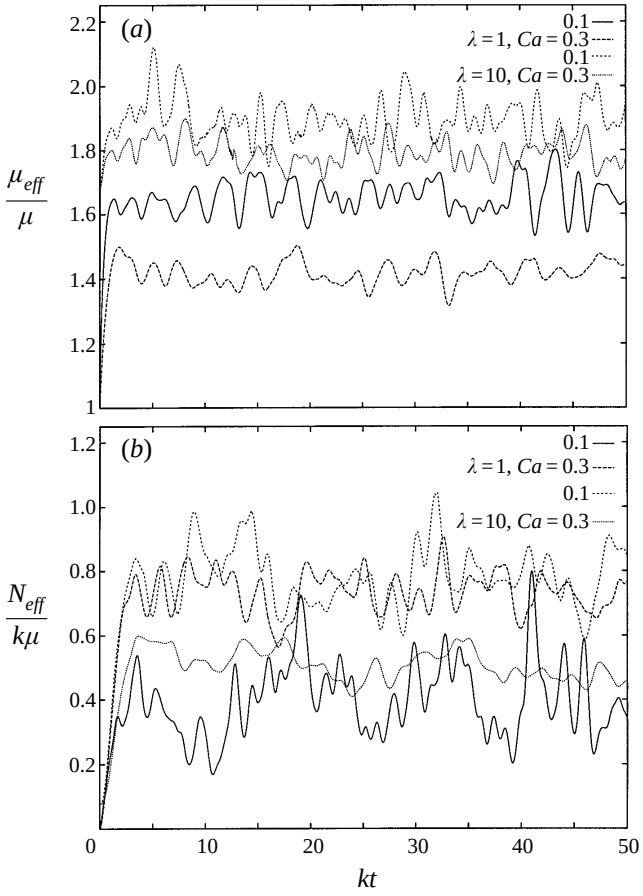

FIGURE 8. Evolution of the suspension effective viscosity and normal-stress difference for the four case studies shown in figure 6.

viscosity: The particles are able to deform in order to accommodate their neighbours, and the suspension behaves like a shear-thinning medium. For all four sets of conditions, the normal stress difference curves rise from the value of zero and then fluctuate around well-defined mean values.

For $\lambda = 1$, the average value of the normalized viscosity μ_{eff}/μ for $Ca = 0.1$ or 0.3 is, respectively, equal to 1.65 or 1.42. These values are somewhat lower than those reported by Li *et al.* (1966) for $\phi = 0.4$, as expected, and in excellent agreement with the values reported by Toose (1997). Loewenberg & Hinch (1996) report the corresponding higher values 2.5 and 1.5 for suspensions of three-dimensional drops at the volume fraction of 0.30 at these capillary numbers. An explanation for the noticeable quantitative differences at the low capillary number $Ca = 0.10$ is elusive.

Increasing the viscosity ratio from 1 to 10, while holding the capillary number constant, raises the mean value of the effective viscosity by a factor of approximately 1.2. As the viscosity ratio becomes larger, the drops become more rigid and the effective viscosity tends to that of a random suspension of freely-suspended circular cylinders. The simulations of Brady & Bossis (1985) for mono-layered suspensions of rigid spheres at volume fraction 0.3 predict an effective viscosity nearly equal to 2μ, which is surprisingly close to the mean value for $\lambda = 10$ shown in figure 8(*a*). The effects are seen clearly in the third column of table 1.

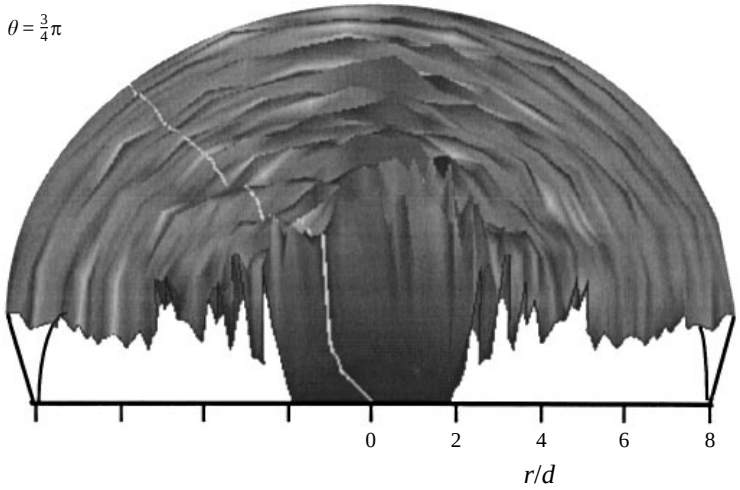

FIGURE 9. A three-dimensional perspective of the pair distribution function $g(r, \theta)$ for $\lambda = 10$ and $Ca = 0.1$, with the slice along $\theta = \frac{3}{4}\pi$ highlighted.

Figure 8(*b*) shows that increasing the capillary number, while holding the viscosity ratio constant, has a mixed influence on the first normal stress difference. For $\lambda = 1$, the normal stress difference rises as the capillary number is increased; whereas for $\lambda = 10$, it is reduced. Increasing the viscosity ratio while holding the capillary number constant also has a mixed influence. As λ is raised, the effective normal stress difference rises at the low capillary number, and drops for the higher capillary number. This behaviour is nevertheless consistent with the results of Zhou & Pozrikidis (1993*a*) for a single file of drops in plane Couette flow. For $\lambda = 1$, these authors found that the normal stress difference increases monotonically as the capillary number is raised, whereas for $\lambda = 10$ they found that it increases from zero, it peaks, and then it decreases and tends to an asymptotic limit. The mixed effect just begins to show in the fourth panel figure 12 of Loewenberg & Hinch (1996) for a suspension of three-dimensional drops at the highest viscosity ratio considered, $\lambda = 5$.

5.3. *Drop-centre pair distribution function*

To describe the geometrical arrangement of the suspended phase, we use the drop centre pair distribution function $g(r, \theta)$ defined in §2.3. In figure 9, we present a typical three-dimensional graph of $g(r, \theta)$ for one of the four cases considered, $\lambda = 10$ and $Ca = 0.1$. In figure 10, we present graphs of g with respect to r for $\theta = 135°$; the upper graph is for $\lambda = 1$ and the lower graph for $\lambda = 10$. To illustrate the effect of λ at a fixed capillary number, in figure 11 we present graphs of g with respect to r at $\theta = 135°$; the upper graph is for $Ca = 0.3$ and the lower graph for $Ca = 0.1$. The angular ray $\theta = 135°$, corresponding to the compressive eigenvector of the rate of strain tensor of the simple shear flow, carries the most information on the relative drop distribution.

First, we examine the effect of the capillary number with reference to figure 10. For $\lambda = 1$ and $Ca = 0.1$, the graph of g shows a sharp peak at a value that is slightly less than $r = 2a$, and a secondary peak at a value that is slightly less than $4a$, as illustrated in figure 10(*a*). This behaviour suggests the clustering of up to three drops in this orientation, with a good probability. Raising the capillary number in this case shifts the radial location of the first peak inward to a value of about $1.5a$, and that of the second and third peaks to $3.0a$ and $4.5a$. The higher the capillary number, the more drops can

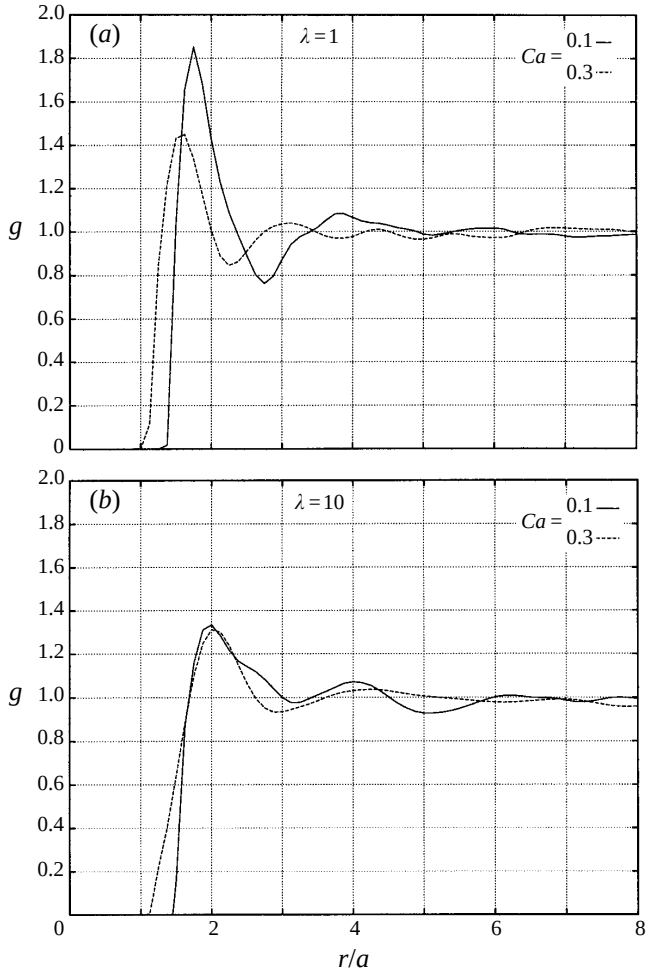

FIGURE 10. Effect of Ca on the drop centre pair distribution function g plotted as a function of r for $\theta = \frac{3}{4}\pi$, $Ca = 0.1$, 0.3 and (a) $\lambda = 1$, (b) 10.

squeeze together to form a structure along this orientation. For $\lambda = 10$, the effect of the capillary number is not quite so dramatic, as illustrated in figure 10(b). Although the radial position of the first peak is approximately equal to $2a$ for both capillary numbers, the secondary peak at $4a$ is much more clearly defined for the lower capillary number. A third peak at the radial distance $6a$ appears for the low capillary number, but the reliability of the results is questionable at this high value of r.

Figure 11 shows that increasing λ while holding the capillary number constant shifts the radial position where g starts taking non-zero values away from the origin and toward the rigid-particle limit $2a$. In addition, it causes the local peaks to be shifted toward larger values of r, and results in fewer but better defined secondary peaks, the first two of which are located at the first two multiples of the radial position of the first peak. In both cases, the radial distance at which peaks can be identified is no greater than $5a$. The results for $\lambda = 10$ are similar to those reported by previous authors for suspensions of rigid spheres and, in particular, by Brady & Bossis (1988). The graphs in figures 10 and 11 illustrate how the character of suspension changes from emulsion-type to suspension-type by altering the fluidity of the suspended phase.

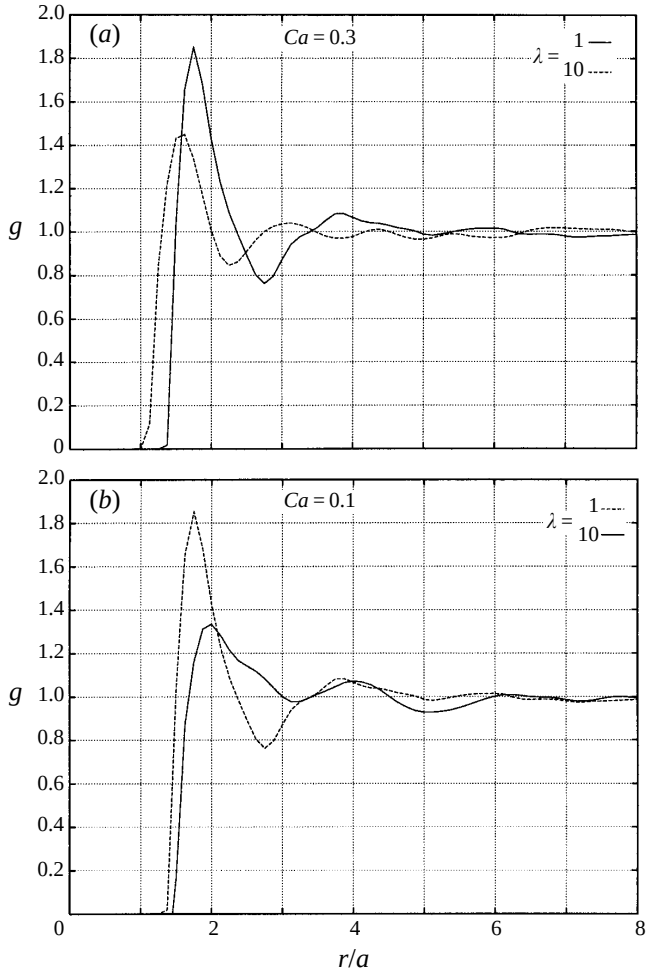

FIGURE 11. Effect of λ on the drop centre pair distribution function g plotted as a function of r for $\theta = \frac{3}{4}\pi$, $\lambda = 1$, 10 and (*a*) $Ca = 0.3$, (*b*) 0.1.

5.4. *Particle clusters*

The significance and consequences of cluster formation on the dynamics of a dense suspension of rigid particles have been described extensively by several authors (e.g. Brady & Bossis 1988; Chang & Powell 1993). In contrast, their role, or even a way for computing cluster size, in suspensions of liquid drops have not been decided. In the case of suspensions of rigid particles, the random motion of the particles and the development of strong lubrication forces at close proximity causes the particles to form long-lived structures and the effective viscosity of the suspension to increase, and is responsible for shear-thickening behaviour. Brady & Bossis (1985) showed that the lubrication forces scale directly with the cluster size.

Computations of cluster size in suspensions of spherical particles have typically employed a criterion for the association of a particle with a cluster, that the particle centre-to-centre separation be less than 2.02 the particle radii. For liquid drops, this criterion could no longer involve a constant inter-drop distance. Li *et al.* (1996) considered two different methods of cluster association based on the minimum separation distance between the interfaces. The first method uses a threshold involving

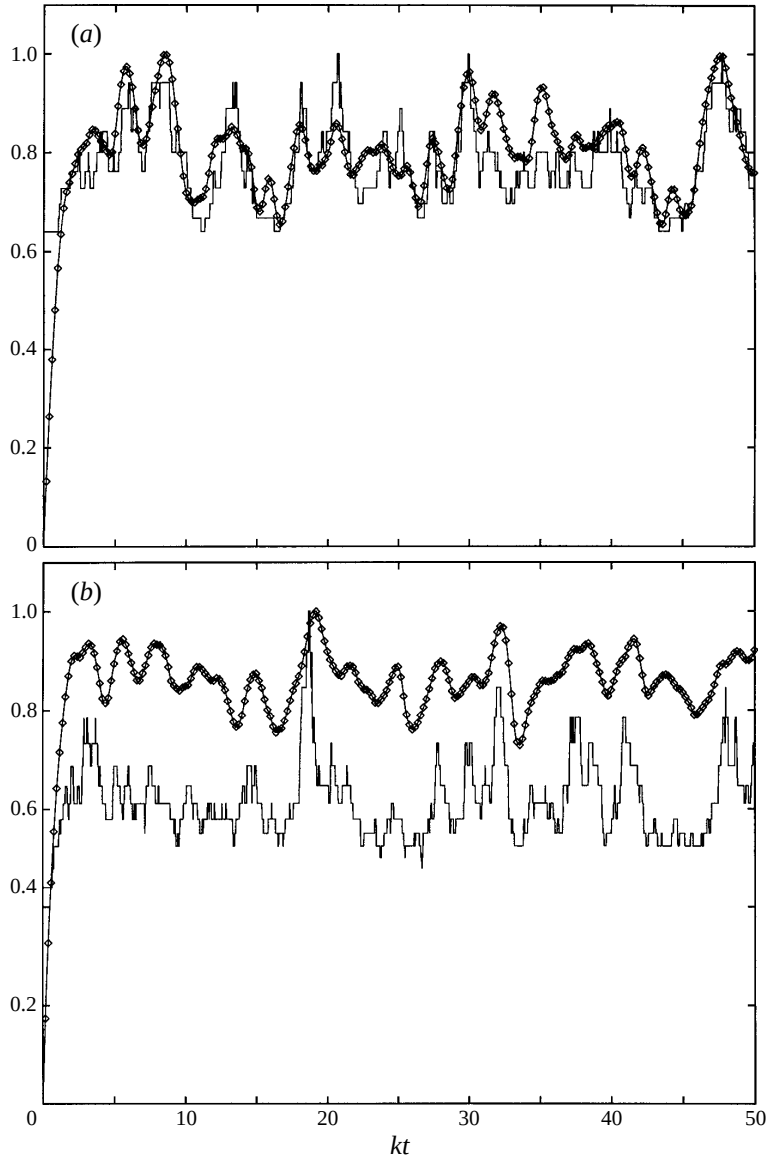

FIGURE 12. Comparison of the normalized drop deformation parameter, averaged over all drops, and normalized average cluster size for (*a*) $\lambda = 10$, $Ca = 0.1$ corresponding to the least deformable drops, and (*b*) $\lambda = 1$, $Ca = 0.3$ corresponding to the most deformable drops. The symbol $\diamond$ represents $\langle D\rangle/\langle D\rangle_{max}$, and the solid line represents $\langle s\rangle/\langle s\rangle_{max}$.

the instantaneous average deformation $\langle D\rangle$, with a value $(0.15+\langle D\rangle)\,a$; the second method uses a constant separation threshold value of $0.30a$, where a is the initial radius of the circular drops. There was no clear consensus as to which, if any, was the best choice. The first method seemed to produce results that qualitatively tracked fluctuations in the instantaneous effective viscosity, which is desirable. On the other hand, when the cluster sizes were averaged over all times, the second method produced a cluster size that is a decreasing function of the capillary number.

Further consideration of the efficacy of the method for cluster definition based on particle separation indicated that the previous two measures are unnecessarily

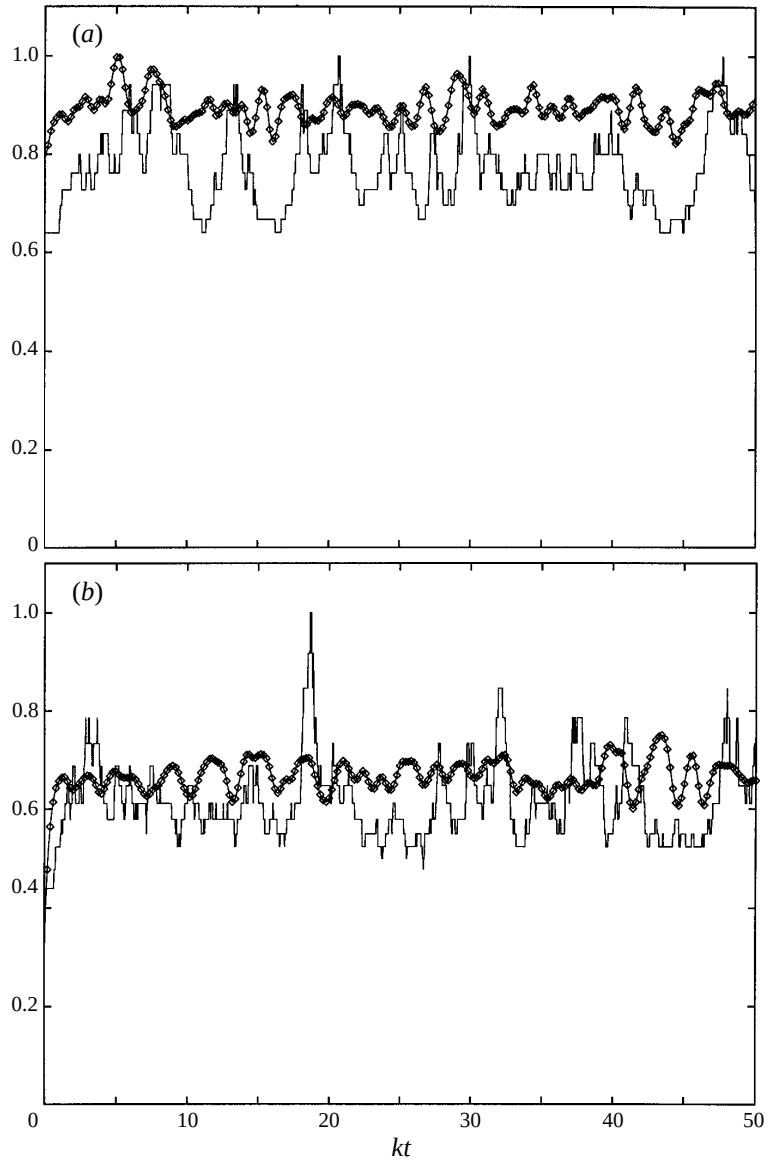

FIGURE 13. Comparison between the normalized effective viscosity and normalized average cluster size for (*a*) $\lambda = 10$, $Ca = 0.1$ corresponding to the least deformable drops, and (*b*) $\lambda = 1$, $Ca = 0.3$ corresponding to the most deformable drops. $\diamond$, normalized and shifted effective viscosity $\mu_{eff}/(\mu_{eff})_{max} - \frac{1}{4}$, ——, average cluster size $\langle s \rangle / \langle s \rangle_{max}$.

conservative. Their inception was motivated by concerns that, for highly deformed drops, situations might arise where the drops would be oriented end-to-end along their major axes, and thus incorrectly be excluded from the cluster based on a criterion based upon drop centre-to-centre separation. The results presented in this section show that even highly deformed drops at close approach rotate to accommodate the presence of their neighbours. With these considerations in mind, we performed cluster size calculations using a threshold value for the centre-to-centre separation 2.02 times the initial drop radii to associate a given drop with other nearby drops in a cluster.

In figure 12, we plot the evolution of the mean cluster size $\langle s \rangle$ for the most rigid

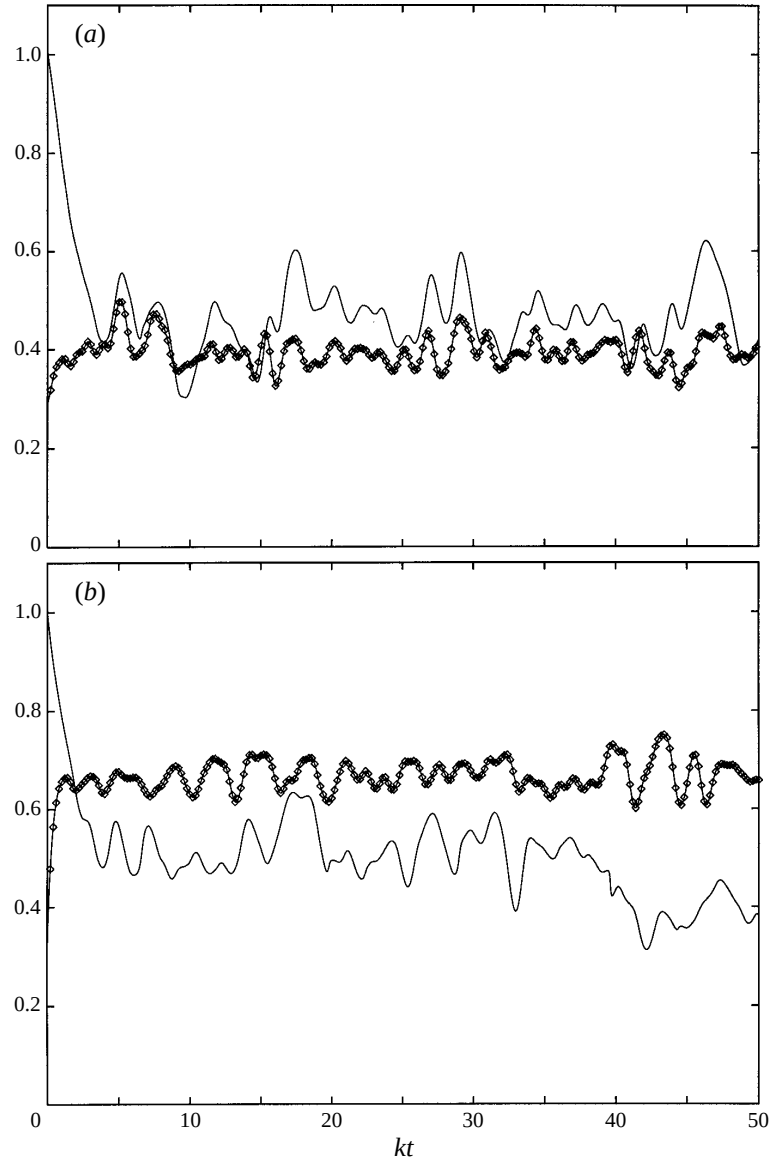

FIGURE 14. Comparison of the normalized average drop inclination angle and normalized effective viscosity for (*a*) $\lambda = 10$, $Ca = 0.1$ corresponding to the least deformable drops, and (*b*) $\lambda = 1$, $Ca = 0.3$ corresponding to the most deformable drops. $\diamond$, average normalized drop inclination angle $\langle\alpha\rangle.\langle\alpha\rangle_{max}$, ——, normalized and shifted effective viscosity $\mu_{eff}/(\mu_{eff})_{max} - \frac{1}{2}$.

and least deformable drops corresponding to $\lambda = 10$, $Ca = 0.1$, and for the least rigid most deformable particles corresponding to $\lambda = 1$, $Ca = 0.3$, and compare it with the evolution of the mean drop deformation. In figure 13, we compare the evolution of the mean cluster size with the evolution of the effective viscosity. It is most interesting to observe the behaviour of the most rigid and least deformable drops in figure 12(*a*), where we note a strong correlation between the cluster size and average drop deformation. In figure 14, we compare the evolution of the average drop orientation angle and effective viscosity, and note a similar strong correlation. It is most interesting that the correlated peaks of drop inclination and effective viscosity in figure 14 are out

Ca	λ	$\langle \bar{s} \rangle$	$\bar{D}_{yy}/a^2k$
0.1	1.0	1.298	0.0279
	10.0	1.199	0.0152
0.3	1.0	1.402	0.0144
	10.0	1.260	0.0113

TABLE 3. Time-average cluster size and drop hydrodynamic diffusivities for a random suspension with 25 drops per periodic box

of phase with the correlated peaks of the drop deformation and cluster size shown in figure 12.

Certain physical mechanisms can be deduced from these results. A deformable drop in an aggregate rotates readily in an attempt to accommodate its neighbours, as well as elongates to allow for maximum packing. The ability of the drops to accommodate each other reduces the effective viscosity of the suspension, as indicated by the phase lag between the fluctuations of the effective viscosity and those of $\langle s \rangle$ in figure 13(*a*). One may then argue that the established correlation between cluster size and effective viscosity in suspensions of rigid spherical particles can be attributed to the inability of the particles to accommodate each other by deformation. Non-spherical particles can accommodate each other by rotation, and this suggests that suspensions of elongated rigid particles behave in many respects differently than suspensions of rigid spheres.

The cluster size and average drop deformation for the least rigid and most deformable drops with $\lambda = 1$ and $Ca = 0.3$, shown in figure 12(*b*), show a good correlation, but the average drop inclination has de-correlated with the effective viscosity, as shown in figure 14(*b*). In fact, the correlation between the average drop deformation to cluster size can be argued to be qualitatively better than that for the most rigid drops with $\lambda = 10$ at $Ca = 0.1$. At one end of the spectrum, $\lambda = 10$ and $Ca = 0.1$, stresses in the flow are dealt with by drop rigid-body translation and rotation and then by deformation. At the other extreme, $\lambda = 1$ and $Ca = 0.3$, the suspended drops lack the interfacial rigidity necessary for coherent rotation and react primarily through deformation. Unlike in suspensions of rigid particles where there is a direct connection between cluster formation, build-up of inter-particle lubrication forces and rise in the effective viscosity, there is no definitive correlation between the effective viscosity and the drop cluster size in suspensions of deformable drops.

Time-average values of the mean cluster size $\langle \bar{s} \rangle$ are given in table 3. The values for the most rigid drops are in excellent agreement with those reported previously for spherical particles by Chang & Powell (1993, figure 12).

5.5. *Drop hydrodynamic diffusivity*

When observed at a sequence of time intervals that are large compared to the inverse shear rate, the seemingly random motion of a tagged drop can be described in terms of an effective hydrodynamic diffusivity tensor $\boldsymbol{D}$ which is defined in terms of the dyadic variance of the drop-centre displacement; that is, the second-order tensor product of the drop-centre displacement from the unperturbed path, $\boldsymbol{X}$ (e.g. Li *et al.* 1996; Davis 1996). As kt tends to infinity, the transverse component of $\boldsymbol{D}$ is given by the common limit of the ratios

$$D_{yy} = \frac{\langle Y^2(t) \rangle}{2t} = \frac{\langle X(t)\, Y(t) \rangle}{kt^2} = \frac{\langle X^2(t) \rangle}{\frac{2}{3}k^2t^3}, \tag{5.1}$$

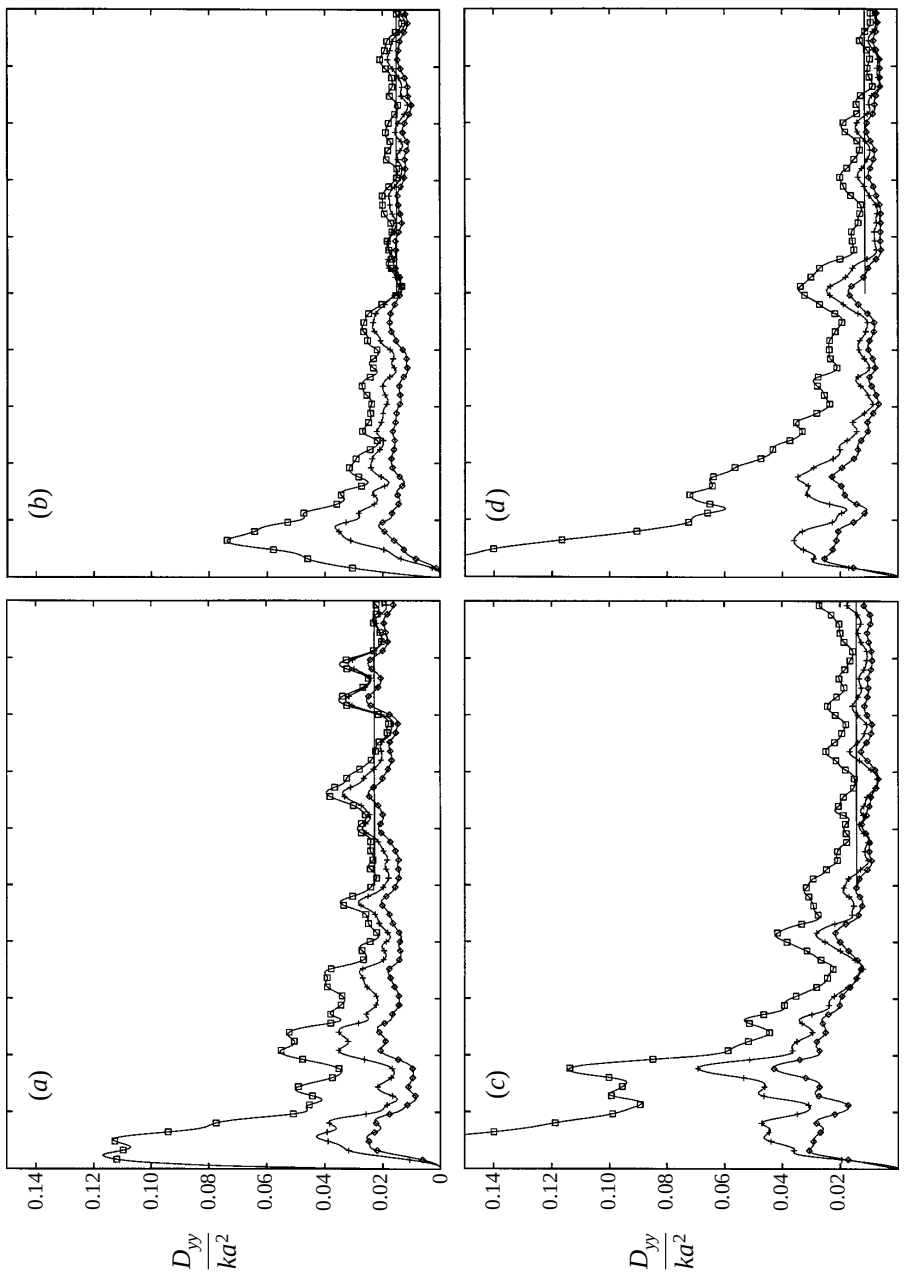

FIGURE 15. Estimates of the lateral component of the hydrodynamic drop diffusivity D_{yy} obtained from the long-time behaviour of $\diamond, \langle Y'^2(t)\rangle/(2t)$; $+, \langle X(t)Y(t)\rangle/(kt^2)$; $\square, \langle X'^2(t)\rangle/[(\frac{8}{3})k^2t^3]$, for (*a*) $\lambda = 1$, $Ca = 0.1$; (*b*) $\lambda = 1$, $Ca = 0.3$; (*c*) $\lambda = 10$, $Ca = 0.1$; (*d*) $\lambda = 10$, $Ca = 0.1$. The horizontal lines show the average over the time period covered.

where the angle brackets designate instantaneous averages over all particles. In figure 15, we plot the three ratios shown in equation (5.1) for the four cases considered in the simulations. Averaging the results over the time period between $25kt$ and $50kt$ yields the horizontal lines. Although 25 particles are hardly enough for the diffusivity to be computed with adequate precision, some trends can be noted. Li *et al.* (1996) found that even with 49 particles, the results are still subject to a substantial amount of statistical uncertainty.

Time-average values for the diffusivity are shown in table 3. As the capillary number is raised from 0.1 to 0.3, the mean value of D_{yy} decreases from 0.0279 ka^2 to 0.0152 ka^2 for $\lambda = 1$, and from 0.0144 ka^2 to 0.0113 ka^2 for $\lambda = 10$. This behaviour is in agreement with that reported by Li *et al.* (1996) for $\phi = 0.40$ and $\lambda = 1$. Holding the capillary number constant and increasing the viscosity ratio reduces the value of D_{yy} for both $Ca = 0.1$ and 0.30. This trend indicates once more that in this limit the suspension tends to exhibit a solid-particle-like behaviour. The diffusivity of rigid particles is lower than that of liquid drops at all volume fractions.

6. Discussion

The significance of the suspended-phase viscosity considered in this work provides us with a vehicle for isolating the effect of particle fluidity, but not for separating it from the effect of interfacial mobility. As the viscosity ratio is raised, the drops become less deformable and behave like rigid bodies. The effect of interfacial mobility, pertinent to readily deformable drops with totally or partially immobilized interfaces and liquid capsules enclosed by thin membranes, has not been examined, although solitary capsules enclosed by elastic membranes have been studied as models of red blood cells (e.g. Barthès-Biesel & Rallison 1981; Ramanujan & Pozrikidis 1998). The effect of interfacial mobility could be investigated best by considering suspensions of capsules enclosed by inextensible but readily deformable membranes with negligible resistance to bending, resembling paper sheets. Biological cells with bi-lipid interfacial layers fall in this category. Unfortunately, the numerical simulation of the motion of such capsules is challenged by numerical instabilities that are manifestations of wrinkling under compression (Zhou & Pozrikidis 1995).

The development of efficient simulation methods is a prerequisite for further studies with more complex particles, such as the ones described in the last paragraph. We have investigated the implementation of the method of interfacial dynamics on computers with parallel-processor architecture. The kernel of the evaluation procedure for equation (2.1) is an N-body type calculation which has typically shown excellent performance in parallel computation. A preliminary implementation of the method has shown excellent speed-up; in this case, the parallelism is based upon the granularity at the level of an individual drop. One requirement is that the interpolation tables for the computation of the Green's function are readily accessible by the individual processors.

The use of interpolation tables transforms the problem of evaluating a long series of expressions to the problem of retrieving relevant quantities from the computer memory, and then performing the simple task of trilinear interpolation. Although responsible for a speed-up of orders of magnitude in computation time, this shift in evaluation is an impediment to efficient use of the machine as the computation becomes memory-bounded. Any further significant increase in the size of the physical system will result in eventual degradation of the performance where most of the run time will be wasted in the CPU to access the system memory. With the advent of massively-parallel computers with sufficiently large local memory, it should now be possible to

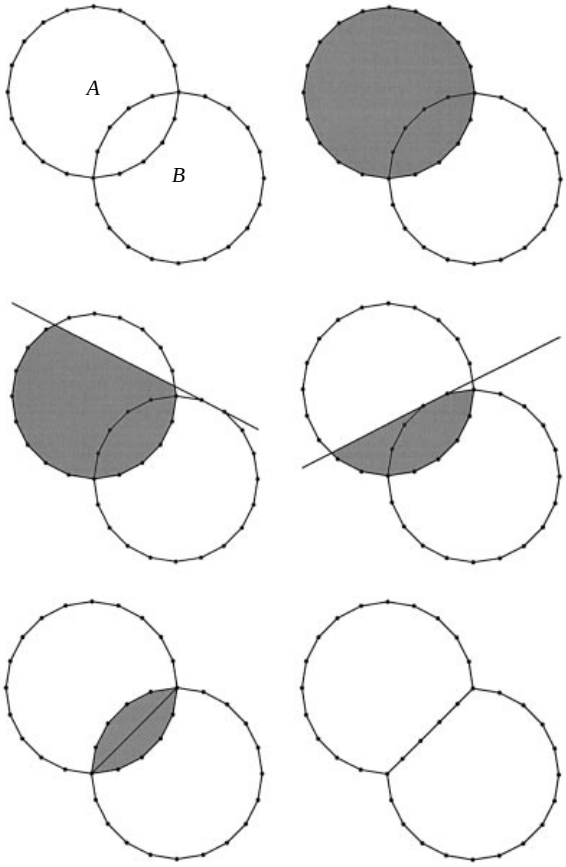

FIGURE 16. Detection of the mutual interface of two overlapping polygons. The area of overlap is identified with the polygonal area A, and then reduced by computing the intersections of the straight lines that are extension of the sides of polygon B with polygon A.

load the interpolation tables onto the local memory of each node and then to perform calculations where memory contention is correspondingly reduced. The field of computer simulation of suspensions of deformable particles in domain with complex geometries will greatly benefit from these hardware advances.

This work was supported by the National Science Foundation, the SUN Microsystems Corporation, and the San Diego Supercomputer Center. Acknowledgement is made to the Donors of the Petroleum Research Fund, administered by the American Chemical Society, for partial support of this research. Computing time was provided by the San Diego Supercomputer Center. Special thanks are extended to C & C Engineering.

Appendix. Numerical deformation of two intercepting drops

Numerical inaccuracies due to timestepping cause two intercepting drops at low capillary numbers to artificially coalesce at a finite time. Interface crossing does not appear when the timestep is reduced to a sufficiently low level either manually or automatically using an adaptive method. Unfortunately, even with adaptive

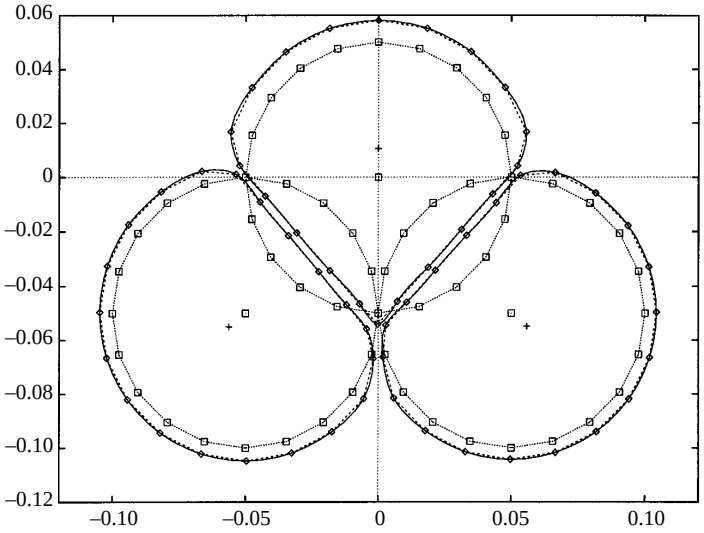

FIGURE 17. Overlap detection, correction, and isotropic expansion of three circular overlapping drops. The dotted lines forming regular polygons outline the overlapping interfaces; the dashed lines connect the modified marker points; and the solid lines show the drop interfaces interpolated with cubic splines. Note that interface repositioning does not change the number of marker points along each interface.

timestepping, the required reduction in step size can be several orders of magnitude smaller than that used when the drops are not in close proximity, and this results in an exorbitant computational cost. Owing to the ability of the drops to deform, artificial coalescence is not observed at higher capillary numbers or lower viscosity ratios.

A numerical method was developed to avoid this difficulty, albeit with a compromise in the physics of the near-contact motion. The algorithm relies on a technique borrowed from computer graphics technology, following Angell & Griffith (1987, pp. 98–102). A more detailed description is provided by Charles (1997). In the first stage, the polygons formed by connecting successive marker points along the interfaces of either one or two drops are tested for possible overlap. Consider the two polygons A and B depicted in the first panel of figure 16. Initially, the polygon of intersection is defined by the entirety of the points defining polygon A, as shown in the second panel of figure 16; the extension of successive sides of polygon B are then tested to reduce the alleged area of intersection, as shown in subsequent panels of figure 16. After the intersection polygon has been found, a slight modification of the procedure described by Angell & Griffith (1987) is used to determine its major diagonal defining the so-called mutual interface of the two original polygons. Up to this point, no action has been taken on the polygon vertices defining the interfaces of the drops. At the next stage, the mutual interface is tested against all segments to modify the interface polygons. If a vertex of a polygon is found to lie on the wrong side of the mutual interface, it is shifted normal to it to produce two touching but non-intersecting polygons. This, of course, results in a reduction in the polygon area for which we compensate.

In our implementation, only pairs of drops whose centre-to-centre spacing was less than three equivalent drop radii were tested for overlap. Each drop pair was tested twice, where the interface of one drop or the other was used to define the test polygon. At the stage of testing for crossing of the polygon and of the mutual interface, the latter

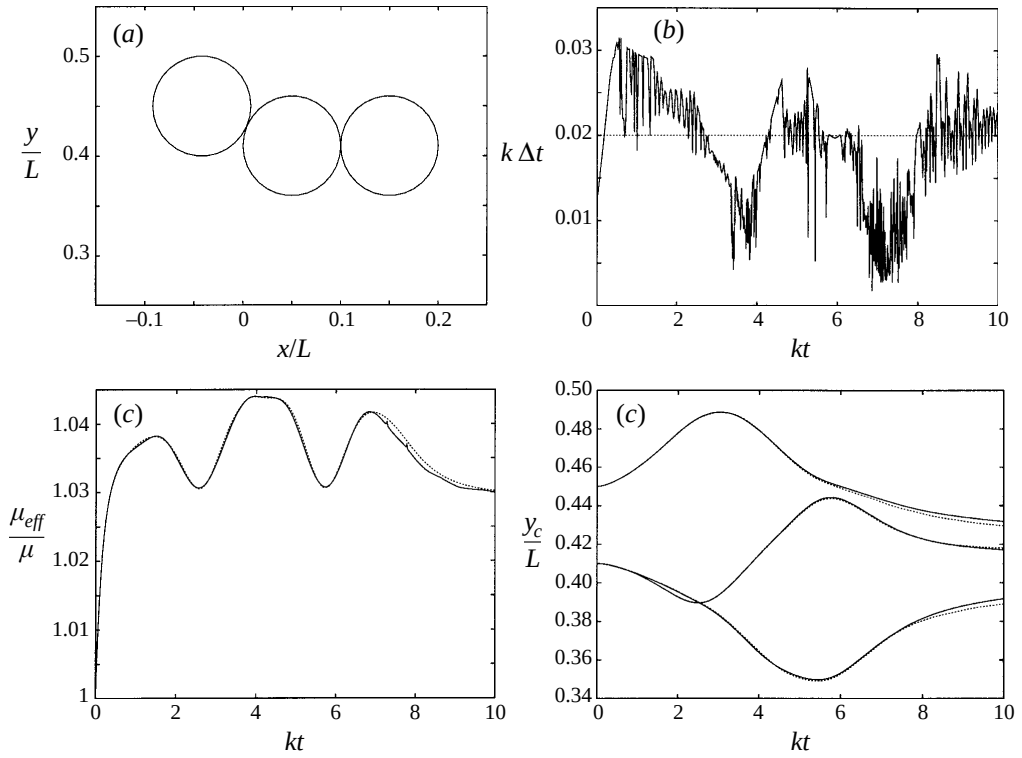

FIGURE 18. Testing of the effect of interface repositioning by a dynamical simulation with three drops. (*a*) Initial configuration of three nearly touching drops; (*b*) size of the timestep determined by an adaptive time-integration method for $\lambda = 1$ and $Ca = 0.0833$ with the interface repositioning module disabled, showing large variations; the horizontal dotted line shows the constant timestep used to test the repositioning method; (*c*) effective viscosity computed with ——, the repositioning method enabled and constant timestep of $k\,\Delta t = 0.02$, – – –, the repositioning method disabled and adaptive timestepping; (*d*) transverse coordinates of drop centres corresponding to (*c*).

was shifted normal to itself by a small distance, typically of the order of $10^{-3}a$, so as to slightly expand the polygon and thus prevent the touching of the polygonal interfaces and the crossing of the interpolated interfaces as described by cubic splines. Finally, all drops were tested for loss of area and isotropically expanded to the proper level when the change in area was found to be larger than 1% the initial value. The procedure was repeated in an iterative manner for all pairs of drops until intersection was not found. An example, illustrating the performance of the method, is presented in figure 17. The dotted lines show the initial interfaces of three overlapping circular drops with the drop centres marked by squares; the dashed lines show the disfigured non-overlapping shapes, with the interface centroids marker by crosses; and the solid lines show the non-overlapping shapes described by cubic splines.

Results of a dynamical simulation for a suspension of three drops per cell for $\lambda = 1$ and $Ca = 0.0833$ are presented in figure 18. At the initial instant, the central drop is nearly touching the two peripheral drops, as shown in figure 18(*a*). The simulation was carried out twice; the first time with the interface repositioning method enabled and a fixed timestep of $k, \Delta t = 0.02$; and the second time with the interface repositioning method disabled and with adaptive timestepping. The large variations of the size of the timestep in the second case are illustrated in figure 18(*b*); the dotted horizontal line

shows the constant timestep. Observing the time histories of the effective viscosity of the suspension and y-position of the drop centres, shown in figure 18(c, d), indicates that a tolerated amount of error is introduced by enabling the interface repositioning method even after a long period of time corresponding to ten inverse shear rates.

REFERENCES

Angell, I. O. & Griffith, G. G. 1987 *High-Resolution Computer Graphics Using FORTRAN 77*. Wiley.

Barthès-Biesel, D. & Rallison, J. M. 1981 The time-dependent deformation of a capsule freely suspended in a linear shear flow. *J. Fluid Mech.* **113**, 251–267.

Bossis, G. & Brady, J. F. 1984 Dynamic simulation of sheared suspensions. I. General Method. *J. Chem. Phys.* **80**, 5141–5154.

Brady, J. F. & Bossis, G. 1985 The rheology of concentrated suspensions of spheres in simple shear flow by numerical simulation. *J. Fluid Mech.* **155**, 105–129.

Brady, J. F. & Bossis, G. 1988 Stokesian Dynamics. *Ann. Rev. Fluid Mech.* **20**, 111–157.

Chang, C. & Powell, R. L. 1993 Dynamic simulations of bimodal suspensions of hydrodynamically interacting spherical particles. *J. Fluid Mech.* **253**, 1–25.

Chang, C. & Powell, R. L. 1994 Self-diffusion of bimodal suspensions of hydrodynamically interacting spherical particles in shearing flow. *J. Fluid Mech.* **281**, 51–80.

Charles, R. 1997 Numerical simulation of the flow of suspensions of liquid drops. Doctoral Dissertation, University of California, San Diego.

da Cunha, F. R. & Hinch, E. J. 1996 Shear-induced dispersion in a dilute suspension of rough spheres. *J. Fluid Mech.* **309**, 211–223.

Davis, R. H. 1996 Hydrodynamic diffusion of suspended particles: a symposium. *J. Fluid Mech.* **310**, 325–335.

Dratler, D. I. & Schowalter, W. R. 1996 Dynamic simulation of suspensions of non-Brownian hard spheres. *J. Fluid Mech.* **325**, 53–77.

Hansen, J. P. & McDonald, I. R. 1986 *Theory of Simple Liquids*. Academic.

Li, X., Charles, R. & Pozrikidis, C. 1996 Simple shear flow of suspensions of liquid drops. *J. Fluid Mech.* **320**, 395–416.

Loewenberg, M. & Hinch, E. J. 1996 Numerical simulation of a concentrated emulsion in shear flow. *J. Fluid Mech.* **321**, 395–419.

Loewenberg, M. & Hinch, E. J. 1997 Collision of two deformable drops in shear flow. *J. Fluid Mech.* **338**, 299–315.

Madanshetty, S. I., Nadim, A. & Stone, H. A. 1996 Experimental measurement of shear-induced diffusion in suspensions using long time data. *Phys. Fluids* **8**, 2011–2018.

Morris, J. F. & Brady, J. F. 1996 Self-diffusion in sheared suspensions. *J. Fluid Mech.* **312**, 223–252.

Pozrikidis, C. 1992 *Boundary Integral and Singularity Methods for Linearized Viscous Flow*. Cambridge University Press.

Pozrikidis, C. 1996 Computation of periodic Green's functions of Stokes flow. *J. Engng Maths* **30**, 79–96.

Pozrikidis, C. 1997 *Introduction to Theoretical and Computational Fluid Dynamics*. Oxford University Press.

Pozrikidis, C. 1998 *Numerical Computation in Science and Engineering*. Oxford University Press.

Ramanujan, S. & Pozrikidis, C. 1998 Deformation of liquid capsules enclosed by elastic membranes in simple shear flow: Large deformations and the effect of capsule viscosity. *J. Fluid Mech.* **361**, 117–143.

Suhs, N. E. & Tramel, R. W. 1991 pegsus user's manual. *Arnold Engineering Development Center Technical Report AEDC-TR-91-8*.

Toose, E. M. 1997 Simulation of the deformation of non-Newtonian drops in a viscous flow. Doctoral Dissertation, Universiteit Twente.

van de Vorst, G. A. L. 1996 Integral formulation to simulate the viscous sintering of a two-dimensional lattice of periodic unit cells. *J. Engng Maths* **30**, 97–118.

Wang, Y., Mauti, R. & Acrivos, A. 1996 The transverse shear-induced liquid and particle tracer diffusivities of a dilute suspension of spheres undergoing a simple shear flow. *J. Fluid Mech.* **327**, 255–272.

Zhou, H. & Pozrikidis, C. 1993*a* The flow of suspensions in channels: single files of drops. *Phys. Fluids* A **5**, 311–324.

Zhou, H. & Pozrikidis, C. 1993*b* The flow of ordered and random suspensions of two-dimensional drops in a channel. *J. Fluid Mech.* **255**, 103–127.

Zhou, H. & Pozrikidis, C. 1995 Deformation of capsules with incompressible interfaces in simple shear flow. *J. Fluid Mech.* **283**, 175–200.